Journal of Materials Science & Technology 65 (2021) 216–227

Contents lists available at ScienceDirect

Journal of Materials Science & Technology

journal homepage: www.jmst.org

Research Article

Faceted Kurdjumov-Sachs interface-induced slip continuity in the eutectic high-entropy alloy, $AlCoCrFeNi_{2.1}$

Ting Xiong[a,b], Wenfan Yang[a,b], Shijian Zheng[a,c,*], Zhaorui Liu[d,e], Yiping Lu[f], Ruifeng Zhang[d,e,**], Yangtao Zhou[a], Xiaohong Shao[a], Bo Zhang[a], Jun Wang[g], Fuxing Yin[c], Peter K. Liaw[h,***], Xiuliang Ma[a,i,*]

[a] Shenyang National Laboratory for Materials Science, Institute of Metal Research, Chinese Academy of Sciences, 72 Wenhua Road, Shenyang 110016, China
[b] School of Material Science and Engineering, University of Science and Technology of China, Hefei 230026, China
[c] Tianjin Key Laboratory of Materials Laminating Fabrication and Interface Control Technology, School of Materials Science and Engineering, Hebei University of Technology, Tianjin 300130, China
[d] School of Materials Science and Engineering, Beihang University, Beijing 100191, China
[e] Center for Integrated Computational Materials Engineering (International Research Institute for Multidisciplinary Science) and Key Laboratory of High-Temperature Structural Materials & Coatings Technology (Ministry of Industry and Information Technology), Beihang University, Beijing 100191, China
[f] Key Laboratory of Solidification Control and Digital Preparation Technology (Liaoning Province), School of Materials Science and Engineering, Dalian University of Technology, Dalian 116024, China
[g] State Key Laboratory of Solidification Processing, Northwestern Polytechnical University, Xi'an 710072, China
[h] Department of Materials Science and Engineering, The University of Tennessee, Knoxville, TN, 37996, USA
[i] School of Material Science and Engineering, Lanzhou University of Technology, Lanzhou 730050, China

ARTICLE INFO

Article history:
Received 11 February 2020
Received in revised form 22 March 2020
Accepted 3 April 2020
Available online 15 July 2020

Keywords:
High-entropy alloy
$AlCoCrFeNi_{2.1}$
Interface
Kurdjumov-Sachs (KS)
Dislocation

ABSTRACT

Recently, the eutectic high-entropy alloy (EHEA), $AlCoCrFeNi_{2.1}$, can reach a good balance of strength and ductility. The dual-phase alloy exhibits a eutectic lamellar microstructure with large numbers of interfaces. However, the role of the interfaces in plastic deformation have not been revealed deeply. In the present work, the orientation relationship (OR) of the interfaces has been clarified as the Kurdjumov-Sachs (KS) interfaces presenting $\left\langle 111\right\rangle_{B2}||\left\langle 110\right\rangle_{FCC}$ and $\left\{110\right\}_{B2}||\left\{111\right\}_{FCC}$ independent of their morphologies. There exist three kinds of interfaces in the EHEA, namely, $(321)_{B2}||(112)_{FCC}$, $(01\bar{1})_{B2}||(33\bar{2})_{FCC}$, and $(23\bar{1})_{B2}||(552)_{FCC}$. The dominating $(321)_{B2}||(112)_{FCC}$ interface and the secondary $(01\bar{1})_{B2}||(33\bar{2})_{FCC}$ interface are both non-slip planes and atomistic-scale faceted, facilitating the nucleation and slip transmission of the dislocations. The formation mechanism of the preferred interfaces is revealed using the atomistic geometrical analysis according to the criteria of the low interfacial energy based on the coincidence-site lattice (CSL) theory. In particular, the ductility of the dual-phase alloy originates from the KS interface-induced slip continuity across interfaces, which provides a high slip-transfer geometric factor. Moreover, the strengthening effect can be attributed to the interface resistance for the dislocation transmission due to the mismatches of the moduli and lattice parameters at the interfaces.

1. Introduction

High-entropy alloys (HEAs) [1,2] have attracted the increasing attention due to their excellent properties, such as high phase stability [3,4], excellent hydrogen storage capacity [5,6], great fatigue property [7,8], and high radiation damage tolerance [9–12]. It is believed that HEAs are the most promising structural materials in the future.

Usually, the most researched HEAs show simple single-phase face-centered-cubic (FCC) or single-phase body-centered-cubic

---

* Corresponding authors at: Shenyang National Laboratory for Materials Science, Institute of Metal Research, Chinese Academy of Sciences, 72 Wenhua Road, Shenyang 110016, China.
** Corresponding author at: School of Materials Science and Engineering, Beihang University, Beijing 100191, China.
*** Corresponding author.
E-mail addresses: sjzheng@imr.ac.cn, sjzheng@hebut.edu.cn (S. Zheng), zrf@buaa.edu.cn (R. Zhang), pliaw@utk.edu (P.K. Liaw), xlma@imr.ac.cn (X. Ma).

https://doi.org/10.1016/j.jmst.2020.04.073
1005-0302/

(BCC) structures [13–16]. While the FCC and BCC HEAs show either the low yield strength (< 400 MPa) or inferior ductility [14,16,17]. Recently, we reported that a eutectic high-entropy alloy (EHEA), $AlCoCrFeNi_{2.1}$, comprising alternate lamellae of soft FCC and hard ordered BCC (B2) phases, can achieve a good balance of strength (yield strength 546.4 MPa, ultimate strength 1046 MPa) and ductility (tensile elongation 17.7 %) [18]. Then, researchers have focused on adjusting the microstructure of $AlCoCrFeNi_{2.1}$ by various thermo-mechanical processes to optimize the mechanical properties [19–21]. For instance, tuning the size of each phase of the eutectic alloys has been applied to optimize the strength [22]. However, the deformation mechanisms of the EHEA have not been understood well. Gao et al. [23] studied the microstructural origins of the high strength and good ductility of the $AlCoCrFeNi_{2.1}$ EHEA from an aspect of the deformation mechanism of each phase, respectively. It was reported that deformation of the $L1_2$ phase was dominated by the planar dislocation gliding on the $\{111\}\langle 110\rangle$ slip systems, and the B2 phase deformed by the dislocation slipping on $\{110\}$ slip planes [23]. But the Burgers vector of dislocations in the B2 phase has not been clarified, and the dislocation interaction with the phase boundaries (interfaces), which exist in large numbers in the EHEA, has yet been revealed.

The interface, in particular, its orientation relationship (OR) and atomic structure, plays an important role in mediating properties of dual-phase materials [24–27]. For example, the interface can mediate the nucleation of dislocations in the adjoining phases [24,25]. Moreover, the interface has important effects on the overall mechanical response of materials, such as the plastic-strain recovery and plastic instability, due to different dislocation interaction mechanisms with the interfaces [26,27]. For the case of the $AlCoCrFeNi_{2.1}$ EHEA, there are high dense inter-phase boundaries (interfaces). A better understanding of the abovementioned characteristics of the interfaces in the eutectic alloys is scientifically and technologically meaningful for designing high-performance EHEAs.

In the present study, we attempt to identify the crystallographic OR and atomic-scale structure of the B2-FCC interface in the EHEA $AlCoCrFeNi_{2.1}$. Furthermore, we explore the effects of the B2-FCC interface on the deformation compatibility and strengthening mechanism in the EHEA $AlCoCrFeNi_{2.1}$.

2. Experimental procedures

The EHEA with the nominal composition of $AlCoCrFeNi_{2.1}$ (elements in atomic ratios) was produced by vacuum induction melting using commercially-pure elements (Al, Co, Ni: 99.9 wt percent (wt.%); Cr, Fe: 99.5 ~ 99.6 wt.%) and casting as described in our previous work [18].

The scanning electron microscopy (SEM) and electron backscattering diffraction (EBSD) observations were conducted, using a Hitachi SU-70 field emission gun scanning electron microscope (FEG-SEM) equipped with an Oxford Nordalys detector. The EBSD samples were prepared by mechanical polishing and then ion etching for 30 min using an LKY-AB ion milling system (Huaye vacuum, Shenyang, China). The EBSD data were acquired with a 100 nm-step size. The EBSD data were analyzed, using the CHANNEL 5 software [28]. The transmission electron microscopy (TEM) observations were performed in a FEI Tecnai G2 F30 TEM and a FEI Titan cube 60–300 TEM operated at 300 kV. The TEM samples after the tensile test were extracted from the tensile specimen tested at room temperature, reported in the our previous work [18].

The nanoindentation experiments were conducted, using a Hysitron tribo-indenter equipped with a diamond Berkovich-shaped indenter. Prior to indentation tests, marks were made with a cross as the coordinate. Indents were mapped as a 2 × 10 pattern with the first indent located at the position (100 μm, -100 μm). Two adjacent indents were spaced ~ 100 μm to avoid the overlapping effect. A maximum load of 5,000 μN was used to minimize the indentation-size effect. The loading time was 15 s. All nanoindentation tests were performed at ambient temperatures. The measured shear moduli of the B2 and FCC phases were obtained from the average elastic-moduli values of the indentations inside each phase according to SEM observation of the as-cast EHEA $AlCoCrFeNi_{2.1}$ sample with the pre-marked coordinate.

To reveal the formation mechanism of the interfaces with specific OR, the atomistic models were built and analyzed by shifting and rotating the single crystal to meet the required OR with the consideration of the maximum coincidence-site lattice (CSL) across the interface [29,30]. In modelling, the experimentally-determined lattice constant of 2.875 Å is used for the B2 structure, while the value of 3.598 Å for the FCC structure. Note that more direct and reliable interfacial energies may be obtained by molecular static/molecular dynamics (MS/MD) simulations, and yet the corresponding interatomic potentials for multicomponent HEAs have not been available so far. Nevertheless, our present geometrical analysis of interfaces may provide a qualitative approximation on the interfacial energy according to the proposed "geometric criteria for the low interfacial energy" by Sutton and Balluffi [31]. To apply this criterion for the present complicated heterogeneous interfaces, some further assumptions are proposed for simplification, and the detailed analysis will be provided in the discussion section. For the visualization of the atomistic-scale structure, we adopted the OVITO program in the present study [32].

3. Results

3.1. Orientation relationship

Basically, the strength and ductility of the interface-dominated materials depend on the interface-dislocation interaction, which is significantly controlled by the interface OR and atomistic structure. To reveal the mechanism for the good balance of high strength and good ductility in the EHEA alloy, we identify the B2-FCC OR first.

The OR between the B2 and FCC phases in the cast EHEA was analyzed by EBSD. Fig. 1(a) is a combined phase image-quality (IQ) map showing the microstructure of the as-cast $AlCoCrFeNi_{2.1}$ EHEA. The eutectic alloy exhibits two typical morphologies: flat lamellae and globular platelets. In Fig. 1(a), the B2 and FCC phases are shown in blue and red, respectively. The average lamellar spacings of the B2 and FCC phases are 1.22 ± 0.58 μm and 2.61 ± 1.21 μm, respectively. Two grains are scanned in Fig. 1(a), and the grain boundary is indicated by a white dotted line. To see the orientation feature, the inverse pole figure (IPF) images of the B2 and FCC phases are displayed in Fig. 1(b). In both grains, the B2 phase maintains an approximately-constant crystallographic orientation with misorientation angles less than 1.5°, while the FCC phase exhibits two different crystallographic orientations with a misorientation angle of 60°, and within each orientation, the misorientation angles are also less than 1.5°, as shown in Fig. 1(c and d). Consequently, there exist two kinds of OR variants for the FCC phase, which will be demonstrated to be twin related by TEM study, referred to as V1 and V2.

The OR of the B2-FCC eutectic was determined by superposing pole figures of the B2 and FCC phases (Fig. 2) corresponding to the right grain in Fig. 1. To show the two variants of the EHEAs clearly, the right grain was rotated simultaneously to make the $[\bar{1}\ 11]_{B2}$ direction parallel to the normal direction of the sample (denoted by Z0), and the $[110]_{B2}$ direction parallel to the horizontal direction of the sample (denoted by X0). The overlap regions of the pole figures are marked with the black color. The crystal-orientation distribution displayed by pole figures in Fig. 2 indicates that the OR of the

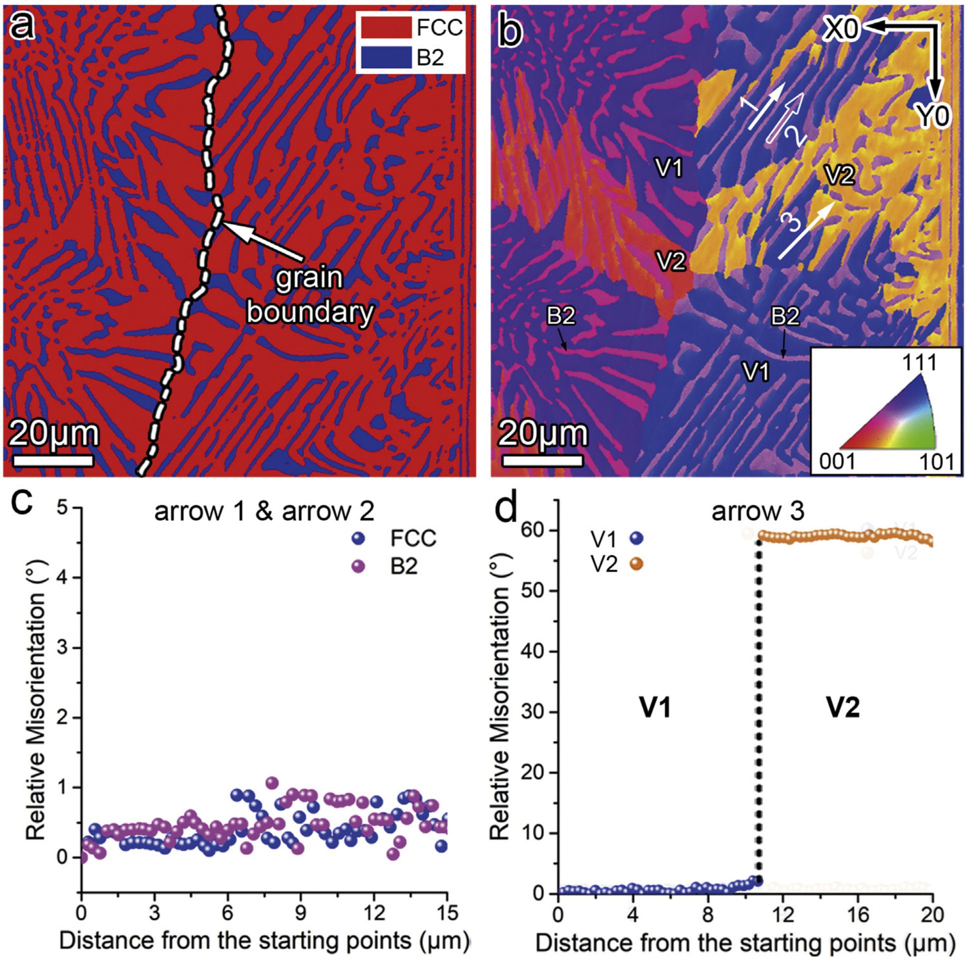

Fig. 1. (a) The combined phase image-quality (IQ) map showing the representative microstructure of the as-cast EHEA. (b) Inverse pole figure (IPF) map along the normal direction of the sample (denoted by Z0) of the as-cast EHEA. (c) The misorientation angles of the point to the starting point along lines 1 and 2 in.(a) inside the FCC and B2 lamellae, respectively. (d) The misorientation angles of the point to the starting point along line 3 in.(a) crossing the two different crystallographic-orientation regions in the FCC phase.

B2-FCC eutectic is $\langle 111\rangle_{B2}||\langle 110\rangle_{FCC}$ and $\{110\}_{B2}||\{111\}_{FCC}$, which are known as KS OR between the FCC and BCC phases [33,34]. As mentioned above, the two crystallographic orientations of the FCC phase in V1 and V2 are twin-related with a misorientation angle of 60°. If V1 is written as $[\bar{1}\,11]_{B2}||[\bar{1}\,10]_{FCC}$ and $(110)_{B2}||(111)_{FCC}$, V2 can be written as $[\bar{1}\,11]_{B2}||[01\,\bar{1}]_{FCC}$ and $(110)_{B2}||(111)_{FCC}$.

3.2. Interface structure

Except for the OR, the atomistic structure of the interface plays a key role in the interface-dislocation interaction too. Fig. 3(a) is a bright-field TEM image and its corresponding composite diffraction pattern of the flat interfaces. The composite diffraction pattern shows the KS OR between the two phases, i.e., $[\bar{1}\,11]_{B2}||[\bar{1}\,10]_{FCC}$ and $(110)_{B2}||(111)_{FCC}$. A simulated composite diffraction pattern based on the KS OR as presented in Fig. 3(c), has been used to identify the interface planes. In this way, the interface planes of the flat lamellae indicated by the yellow-dotted line in Fig. 3(a) are identified to be $(321)_{B2}||(112)_{FCC}$. As for the globular platelets, the OR remains the same as that in the flat lamellar region, as presented by the corresponding composite-diffraction pattern in Fig. 3(b). Typical interfaces of the globular platelets, indicated with yellow and aqua blue dotted lines, are determined to be $(321)_{B2}||(112)_{FCC}$ and $(01\,\bar{1})_{B2}||(33\bar{2})_{FCC}$, respectively.

As mentioned above, there are two OR variants in the as-cast EHEA. The two crystallographic ORs in the FCC phase are demonstrated to be twin-related by TEM analysis. Fig. 4(a) is a bright-field TEM micrograph showing the growth twins in the as-cast EHEA with the composite diffraction pattern of V1, V2, and B2 phases at the top right corner. In particular, the twin relationship in the FCC phase is indicated by the red (V1) and green (V2) patterns, and the blue pattern is corresponding to the B2 phase. To present the two OR variants and their interfaces clearer, a corresponding schematic has been exhibited in Fig. 4(b). The V1, V2, and B2 phases are represented in red, green, and blue, respectively. Thus, owing to the growth twin, there are five kinds of interfaces marked with yellow, black, rose red, orange, and blue dotted lines in Fig. 4(a and b). To identify the interfaces, a simulated composite diffraction pattern of the B2, V1, and V2 phases is presented in Fig. 4(c), in which the arrows perpendicular to the dotted lines indicate the interface planes. The interfaces corresponding to yellow, black, rose red, orange, and blue dotted lines are $(321)_{B2}||(112)_{V1}$, $(321)_{B2}||(255)_{V2}$, $(23\bar{1})_{B2}||(552)_{V1}$, $(23\bar{1})_{B2}||(211)_{V2}$, and $(111)_{V1}||(111)_{V2}$, respectively. Among these interfaces, the $(111)_{V1}||(111)_{V2}$ interface is the twin interface. Due to the high symmetries of the B2 and FCC phases, the $(321)_{B2}||(112)_{V1}$ interface is equal to the $(23\bar{1})_{B2}||(211)_{V2}$ interface, and the $(23\bar{1})_{B2}||(552)_{V1}$ interface is equal to the $(321)_{B2}||(255)_{V2}$ interface. Thus, there exist a small number of $(23\bar{1})_{B2}||(552)_{FCC}$ interfaces in the EHEA alloy, as shown in Fig. 4, due to the growth twins of the FCC phase. In general, $(321)_{B2}||(112)_{FCC}$ is the dominating interface, $(01\bar{1})_{B2}||(33\bar{2})_{FCC}$ is the secondary inter-

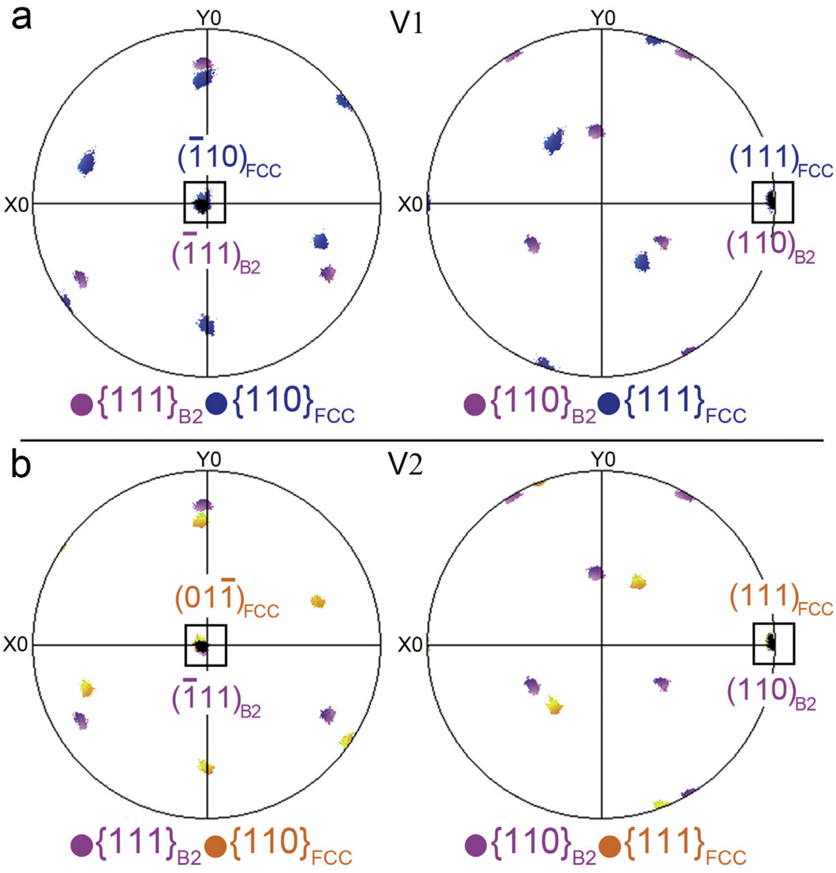

Fig. 2. Overlapped pole figures from the EHEAs within the right grain showing the two variants of the $\langle 111\rangle_{B2}||\langle 110\rangle_{FCC}$ and $\{110\}_{B2}||\{111\}_{FCC}$ OR: (a) V1: $[\bar{1}\ 11]_{B2}||[\bar{1}\ 10]_{FCC}$ and $(110)_{B2}||(111)_{FCC}$; (b) V2: $[\bar{1}\ 11]_{B2}||[01\ \bar{1}]_{FCC}$ and $(110)_{B2}||(111)_{FCC}$. The right grain was rotated simultaneously to make the $[\bar{1}\ 11]_{B2}$ direction parallel to the normal direction of the sample (denoted by Z0) and the $[110]_{B2}$ direction parallel to the horizontal direction of the sample (denoted by X0).

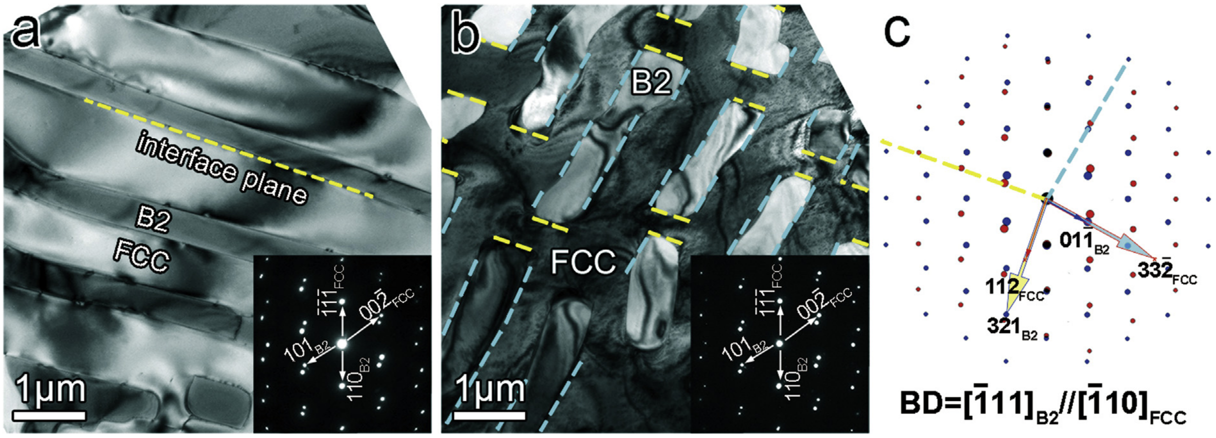

Fig. 3. (a) Flat lamella with the $(321)_{B2}||(112)_{FCC}$ interface indicated with a yellow-dotted line and the corresponding composite diffraction patterns of both phases. (b) Globular platelet morphology showing the same OR presenting the interfaces, $(321)_{B2}||(112)_{FCC}$ and $(01\bar{1})_{B2}||(33\bar{2})_{FCC}$, indicated with yellow and aqua blue dotted lines, respectively. (c) A simulated diffraction pattern of the composite diffraction pattern with the KS OR to determine the exact interface in (a and b).

face, and $(23\bar{1})_{B2}||(552)_{FCC}$ is the least interface in the as-cast EHEA.

To reveal atomistic-scale feature of the dominated interfaces in the EHEA, we conducted the high-angle annular dark-field high-resolution scanning transmission electron microscopy (HAADF-HRSTEM) investigation. Fig. 5 exhibits typical HAADF-HRSTEM images showing the atomistic-scale interfacial structures of the $(321)_{B2}||(112)_{FCC}$ and $(01\ \bar{1})_{B2}||(33\bar{2})_{FCC}$ interfaces, viewed along the $[\bar{1}\ 11]_{B2}||[\bar{1}\ 10]_{FCC}$ direction. The HAADF-HRSTEM images indicate that the interfaces are atomistic-scale faceted. In specific, the $(321)_{B2}||(112)_{FCC}$ interface comprises alternated $(110)_{B2}||(111)_{FCC}$ and $(101)_{B2}||(001)_{FCC}$ facets, and the $(01\ \bar{1})_{B2}||(33\bar{2})_{FCC}$ interface comprises $(110)_{B2}||(111)_{FCC}$ and $(01\ \bar{1})_{B2}||(11\ \bar{1})_{FCC}$ facets. Also, no misfit dislocations are observed at the $(321)_{B2}||(112)_{FCC}$ interface, while one set of misfit dislocations distribute regularly with a spacing of about 1.19 nm at the $(01\ \bar{1})_{B2}||(33\bar{2})_{FCC}$ interface. The misfit dislocations will interact with the deformed dislocations to help strengthen the material, which will be discussed in the discussion section.

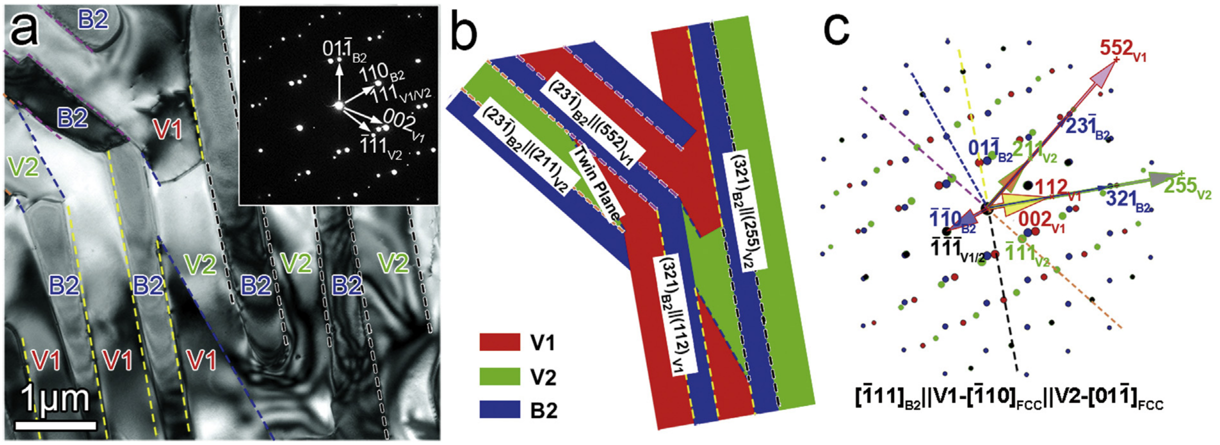

Fig. 4. (a) A bright-field TEM micrograph showing the growth twin in the as-cast AlCoCrFe$Ni_{2.1}$ EHEA with the corresponding composite selected area electron diffraction (SAED) pattern of the B2, FCC matrix (V1), and FCC twin (V2) inset at the top right corner. (b) A sketch map of the corresponding interface planes due to the growth twin in the FCC phase. (c) A simulated diffraction pattern of the composite diffraction pattern with the two KS ORs to determine the exact interfaces formed along with the growth twin.

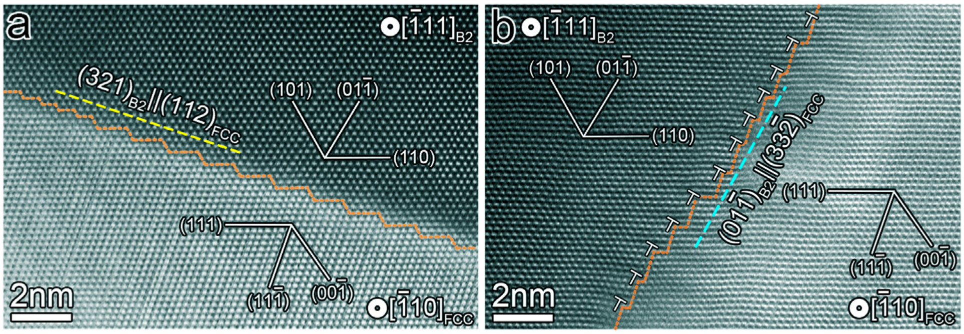

Fig. 5. HAADF-HRSTEM images of (a) $(321)_{B2}||(112)_{FCC}$ and (b) $(01\bar{1})_{B2}||(33\bar{2})_{FCC}$.

Table 1
Invisibility criterion for diffraction and Burgers vectors of the dislocations in the FCC phase of Fig. 6. "√" and "×" represent the dislocation invisibility and visibility, respectively.

Operating reflection	Burgers vectors of dislocations			
	±[110]	±[$\bar{1}$01]	±[101]	±[0$\bar{1}$1]
g = (11$\bar{1}$)	√	√	×	√
g = (1$\bar{1}$1)	×	×	√	√
g = (200)	√	√	√	×
g = (002)	×	√	√	√

3.3. Interface-dislocation interactions during deformation

After clarifying the OR and atomistic structure of the interface, we investigated the interface-dislocation interaction mechanisms of the bi-phase EHEA. The post-mortem TEM characterization was performed, using the diffraction-contrast TEM imaging technique. Fig. 6 presents the typical images of dislocations in the FCC phase. Dislocation glide is strongly localized on a distinct set of {111}-type FCC lattice planes. By applying the ***g***·***b*** = 0 invisibility criterion (Table 1), the Burgers vector of the dislocations was determined to be 1/2 < 110 > . Most of the dislocations are mixed edge and screw dislocations due to the curved line morphology for the same Burgers vector at the same ***g*** vector. Therefore, the plastic deformation of the FCC phase in the EHEA is governed by the planar slip of the 1/2 < 110> dislocation on the {111} planes.

Dislocations in the B2 phase have been identified, as indicated in the bright-field TEM images in Fig. 7. The dislocations display as straight lines with a trace lying on the {110} B2 lattice planes. It has been established that in the B2-structured polycrystal deformed at room temperature, there are two types of Burgers vectors: <111> and <001> [35–37]. We note that the dislocations are visible for ***g*** = (0 $\bar{1}$ 1), ***g*** = (110), and ***g*** = (001) in Fig. 7(a, b, and d). While they are almost out of contrast for the ***g*** = (101) reflection in Fig. 7(c). Based on the ***g***·***b*** = 0 invisibility criterion summarized in Table 2, the dislocations in Fig. 7 can be determined to be with the Burgers vector of [11 $\bar{1}$]. The dislocations in the B2 phase are determined as pure edge or screw dislocations for their straight-line shapes. The exact direction of the dislocation line, ***u***, can be determined by the dislocation traces analysis,

$$\mathrm{u} = \mathrm{g}_1 \hat{\mathrm{g}}_2 \tag{1}$$

where $\boldsymbol{g}_1$ and $\boldsymbol{g}_2$ are the **g** vectors of dislocation trace planes, when the beam directions are $\boldsymbol{B}_1$ and $\boldsymbol{B}_2$, respectively. Hence, the dislocations in the B2 phase are determined to be of a pure screw character with a dislocation-line direction of [11 $\bar{1}$], which is parallel with the Burgers vector. Thus, the primary deformation mode of the B2 phase is associated with the pure screw dislocations, <111> dislocations slip on the {110} lattice planes.

As we have seen that there are large numbers of interfaces in the EHEA, interfaces are believed to play an important role in the plastic deformation. In the initial state of deformation, the numerous interfaces can serve as heterogenous dislocation sources to trigger plastic deformation [38,39]. Due to the intrinsic soft character of the FCC phase, the dislocations are supposed to be emitted into the FCC side from the interfaces to activate the plastic deformation in the FCC phase firstly. Fig. 8(a) shows an array of dislocations in the FCC phase blocked by the interface. While in Fig. 8(b), the slip traces can

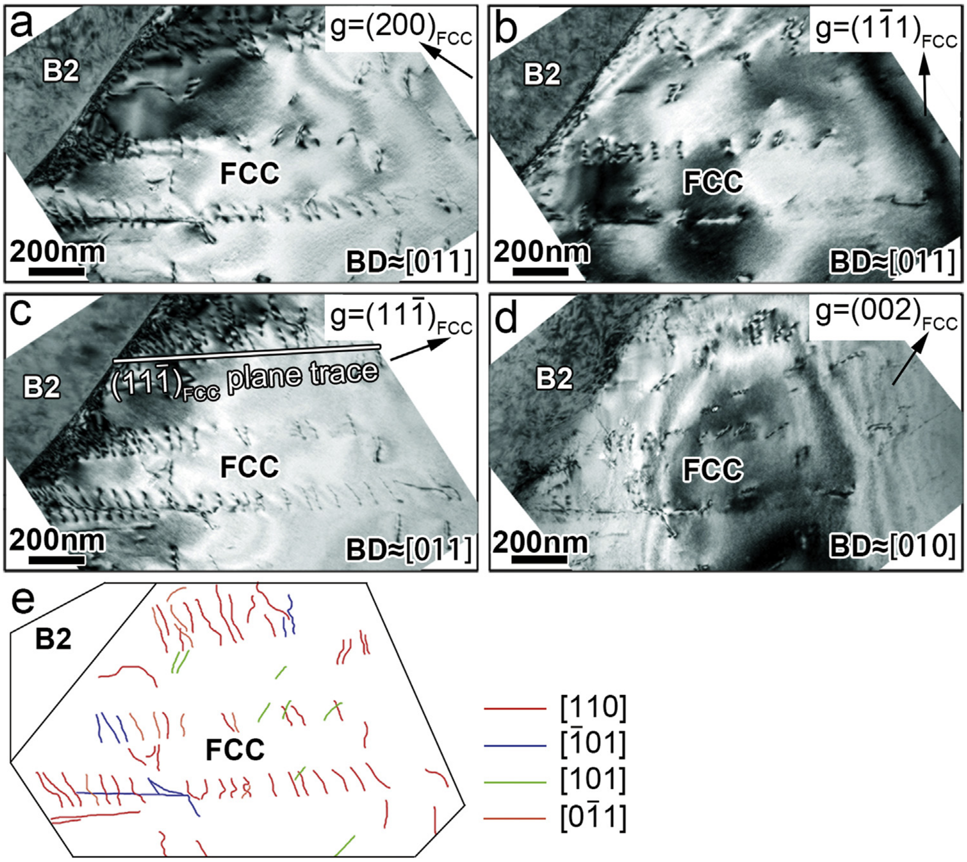

Fig. 6. Dislocation identification using the two-beam diffraction with different **g** vectors in the FCC phase: (a) **g** = (200); (b) **g** = (1 $\bar{1}$ 1); (c) **g** = (11 $\bar{1}$); (d) **g** = (002). The **g** vector is drawn with a black arrow. (e) Tracings of the visible dislocations in (a-d). The different colors distinguished the different Burgers vectors of each dislocation.

Table 2
Invisibility criterion for diffraction and Burgers vectors of the dislocations in the B2 phase of Fig. 7. "√" and "×" represent the dislocation invisibility and visibility, respectively. The Burgers vectors of the dislocations activated in Fig. 7 can be determined to be [11 $\bar{1}$].

Operating reflection	Burgers vectors of dislocations						
	±[111]	±[$\bar{1}$11]	±[1$\bar{1}$1]	±[11$\bar{1}$]	±[100]	±[010]	±[001]
$g = (0\bar{1}1)$	×	×	√	√	×	√	√
$g = (110)$	√	×	×	√	√	√	×
$g = (101)$	√	×	√	×	√	×	√
$g = (001)$	√	√	√	√	×	×	√

be observed in both phases with almost a one-to-one correspondence across the interfaces, which indicate that the dislocation slip can cross the interfaces. The slip traces on $(111)_{FCC}$ are exactly parallel to that on $(110)_{B2}$ while the slip traces on $(11\bar{1})_{FCC}$ and $(01\bar{1})_{B2}$ intersect at the interface with an angle of about 9.5°, as exhibited in Fig. 8(b). Fig. 8(c) is a magnified bright-field TEM image presenting that the FCC dislocations extend into the B2 phase. Accordingly, the interfaces, on one hand, can act as strong barriers for some dislocations, and, on the other hand, are transparent for the others.

4. Discussion

4.1. Atomistic modeling revealing the formation of preferred interfaces in the EHEA

To provide an explanation on the experimental observation that there are three kinds of interfaces, namely the $(321)_{B2}||(112)_{FCC}$, $(01\bar{1})_{B2}||(33\bar{2})_{FCC}$, and $(23\ \bar{1})_{B2}||(552)_{FCC}$ interfaces in the EHEA AlCoCrFeNi$_{2.1}$, and the $(321)_{B2}||(112)_{FCC}$ play the dominating role in this dual-phase alloy, we build the interfaces by keeping the KS orientation and taking $[\bar{1}\ 11]_{B2}||[\bar{1}\ 10]_{FCC}$ as the rotation axis for atomistic modelling.

According to the CSL interface theory [30], partial sites of the two crystal lattices at the two sides of the boundary come into the coincidence at the interface. For an interface between the B2 and FCC phases, an exact coincidence is not generally possible. With the certain applied strain to both lattices, a forced coincidence cell can be achieved, and hence, the periodic boundary conditions can be imposed. As proposed by Sutton and Balluffi [31], a high planar CSL density corresponding to a low energy state is preferred. Under such circumstances, a higher planar CSL-site density corresponds to a lower distance between two periodic parallel or near-parallel atomic columns in upper (d_1) and lower (d_2) crystals within the interface. Hence, as shown in Fig. 9, the interface model is built by only considering both distances between such atomic columns less than 2 nm and the near-parallel planes with the deviation angles less than 5°. Fig. 9(a) illustrates the possible interface configurations satisfying the KS OR, i.e., $[\bar{1}\ 11]_{B2}||[\bar{1}\ 10]_{FCC}$ and $(110)_{B2}||(111)_{FCC}$. Specifically, the nearly-parallel terminated surfaces of the B2 (the upper crystal) and FCC (the bottom crystal) phases forming the

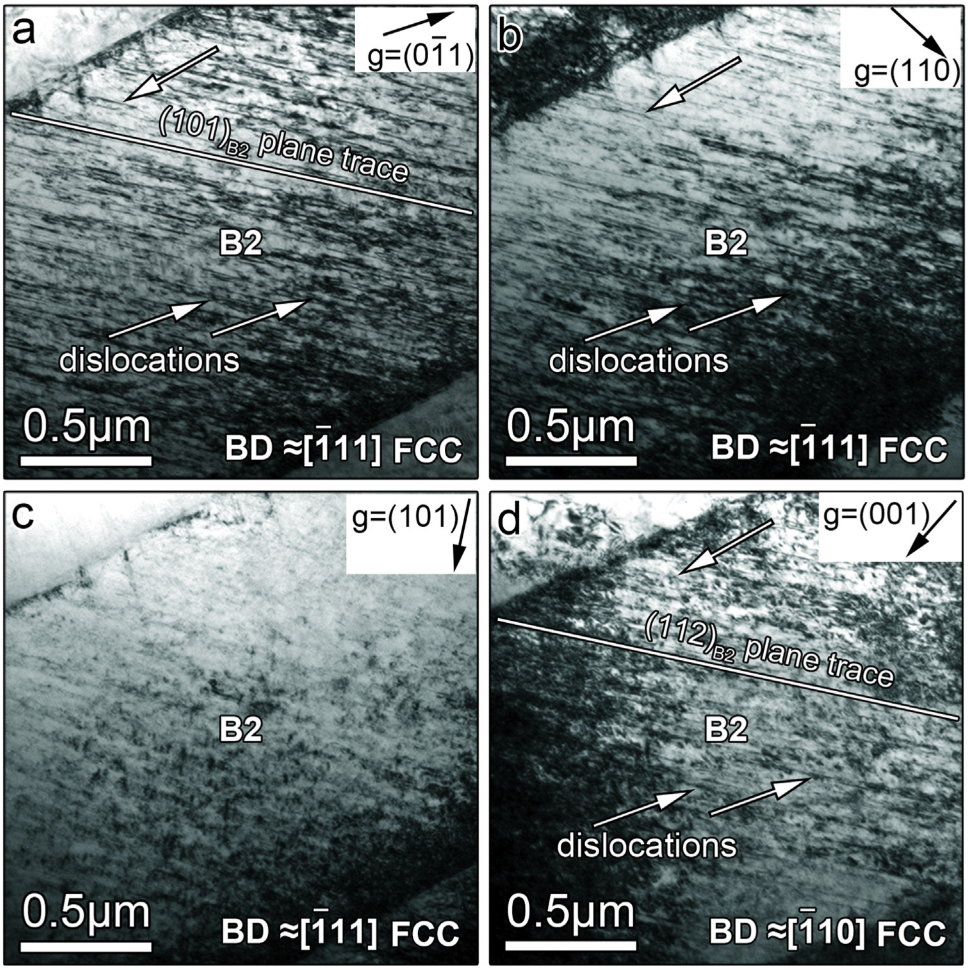

Fig. 7. Pure screw dislocation with the Burgers vector, $[11\bar{1}]$ identification, using the two-beam diffraction with different ***g*** vectors in the B2 phase: a, ***g*** = $(0\bar{1}1)$; b, ***g*** = (110); c, ***g*** = (101); d, ***g*** = (001). The ***g*** vector is drawn with a black arrow. The beam directions of (a), (b), and (c) are near $[\bar{1}11]$, and the beam direction of (d) is near $[\bar{1}10]$.

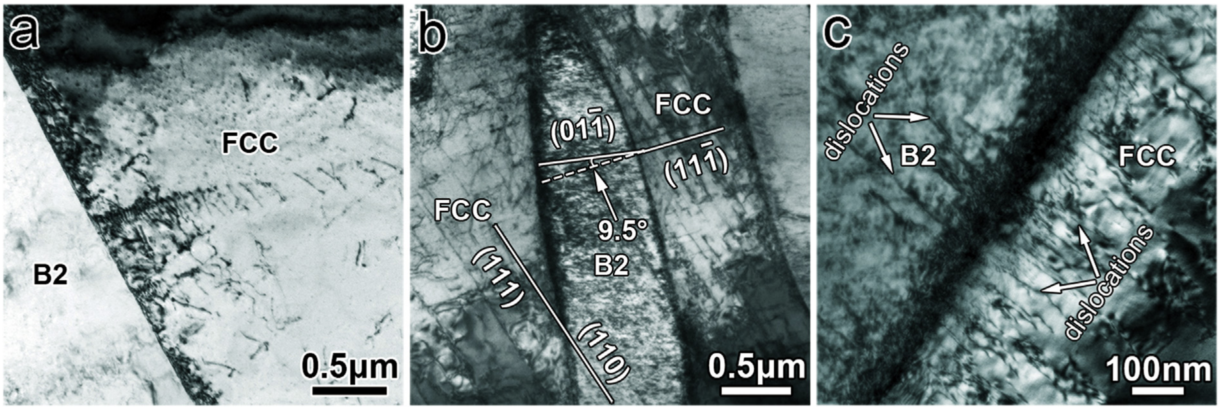

Fig. 8. (a) A bright-field TEM image presenting an array of dislocations piled up at the phase boundary. (b) A bright-field TEM image showing that the continuity of the slip traces in the B2 and FCC phases. (c) A magnified TEM image exhibiting dislocations in the FCC phase extended to the B2 phase.

interface are chosen clockwise from 0° to 180° with respect to the zone axes, $[\bar{1}\,11]_{B2}||[\bar{1}\,10]_{FCC}$. The in-plane lattice mismatch parameter, δ, is defined as,

$$\delta = \min\left(\left|\frac{nd_1 - d_2}{nd_1}\right|, \left|\frac{(n+1)d_1 - d_2}{(n+1)d_1}\right|\right) \tag{2}$$

where d_1 and d_2 stand for the distances between two periodic parallel atomic columns in upper and lower crystals within the interface, respectively, as marked with double-sided arrows between the green and red circles in Fig. 9(c–r), and n gives the multiplication factor of the two parallel atomic rows in order to achieve the minimum lattice mismatch. The in-plane lattice mismatch means the minimum strain needed to be imposed to let the contacting facets between the two crystals create a local minimum inter-planar CSL density, which is used to evaluate the interface energy of a certain orientation without considering the influence of the random solute

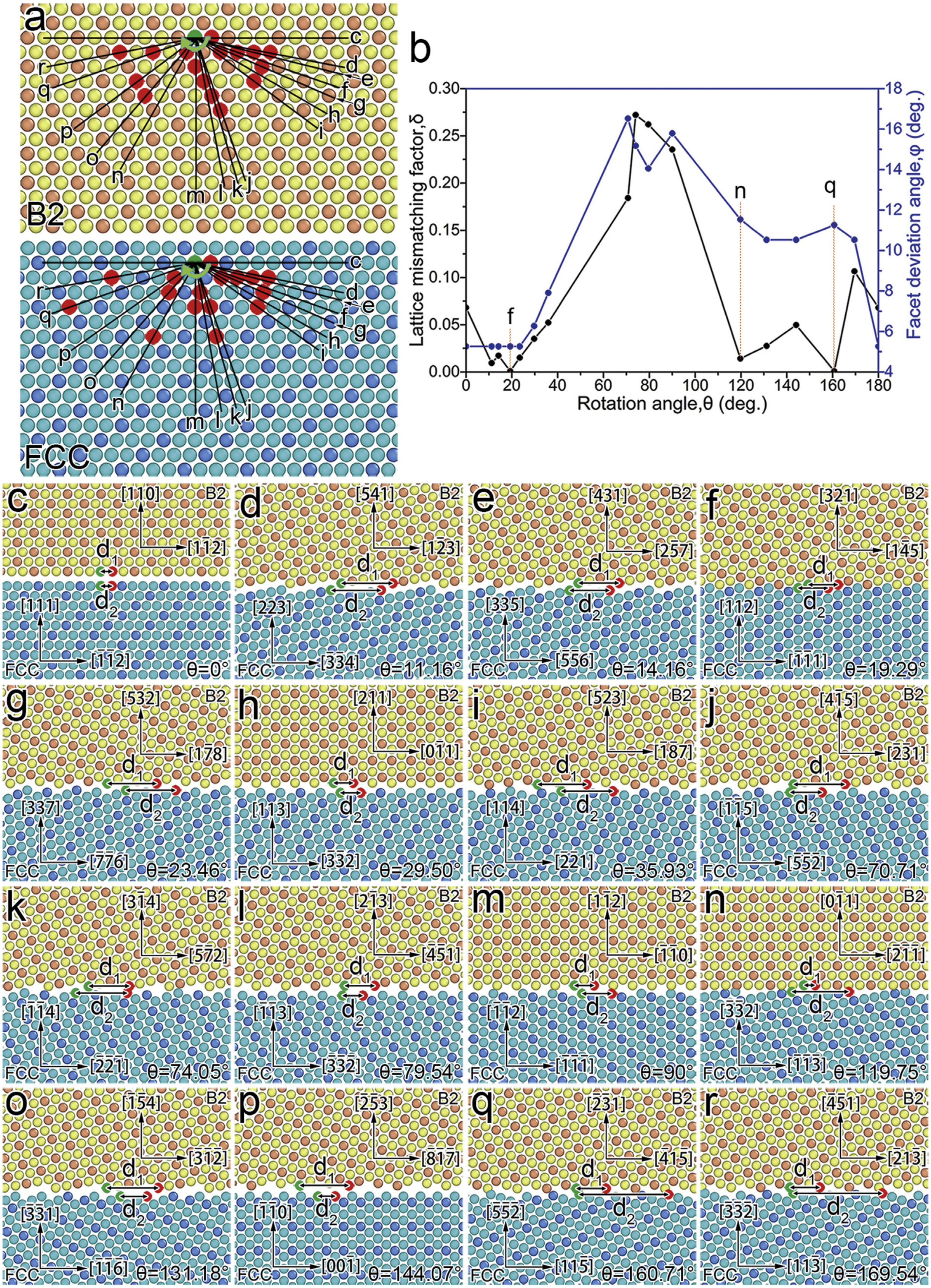

Fig. 9. (a) The nearly-parallel termination interfaces of the B2 (the upper crystal) and FCC structures (the bottom crystal) are chosen to be clockwise rotated with angles from 0° to 180° between the termination interfaces and their respective parallel close-packed atom row of $(110)_{B2}||(111)_{FCC}$. (b) The calculated in-plane lattice mismatch parameter, δ, as well as the facet-deviation angle, φ, along the lateral direction with the variation of the rotation angle, θ. (c-r) The side views of the relaxed structure-atomic configurations when the interface rotated with different rotation angles and with the parallel compact planes in both phases.

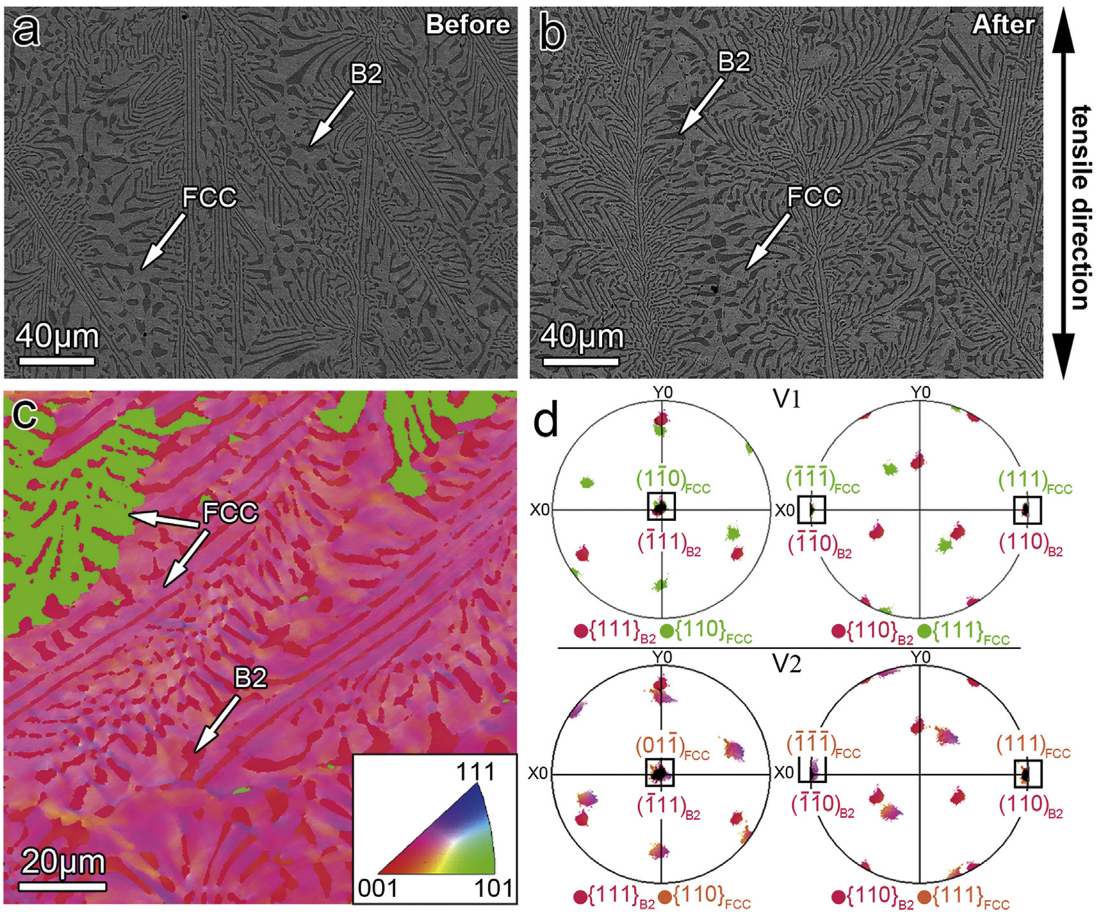

Fig. 10. SEM images of the EHEA (a) before and (b) after the tensile test, showing that no macroscopic strain localization took place during deformation. (c) Inverse pole figure (IPF) map of the as-deformed EHEA. (d) Overlapped pole figures of the B2 and FCC phases in c, indicating that the KS OR remains after the deformation.

distribution in the EHEA. A similar method was used by Sutton and Balluffi in the energy evaluation of the formation of the lock-in row interface structure between two crystals [31], in which a low interface energy can be achieved by forming a high interface CSL density, and therefore, only a low localized strain is needed to reach such a structure.

According to Fig. 9(a), the calculated local lattice mismatches of the interfaces with different rotation angles are presented in Fig. 9(b). Fig. 9(c–r) illustrates the side views of the atomistic configurations of the interfaces with different rotation angles. As mentioned above, it is generally believed that a lower lattice mismatch corresponds to a lower interfacial energy, providing the most favorable crystallographic correspondence between two crystals across the interface. It can be clearly seen from Fig. 9(b) that the interfaces of $(321)_{\mathrm{B2}}||(112)_{\mathrm{FCC}}$ and $(23\bar{1})_{\mathrm{B2}}||(552)_{\mathrm{FCC}}$, presented in Fig. 9(f and q), exhibit the minimum lattice-mismatch parameter value of $\delta = 0.0009$. Furthermore, an additional local minimum lattice-mismatch parameter with the value of $\delta = 0.0142$ is demonstrated for the interface, $(01\bar{1})_{\mathrm{B2}}||(33\bar{2})_{\mathrm{FCC}}$, designated in Fig. 9(n).

However, for assessing the interface formed in the EHEA, the application of the afore-mentioned lattice-mismatch parameter, δ, may be inadequate to fully comprehend the experimentally-observed interfaces. For instance, the $(321)_{\mathrm{B2}}||(112)_{\mathrm{FCC}}$ and $(23\bar{1})_{\mathrm{B2}}||(552)_{\mathrm{FCC}}$ interfaces both with the lowest mismatch parameter value of $\delta = 0.0009$, the $(321)_{\mathrm{B2}}||(112)_{\mathrm{FCC}}$ interface, f, prevails over the $(23\bar{1})_{\mathrm{B2}}||(552)_{\mathrm{FCC}}$ interface, q, in the as-cast EHEA. This trend primarily stems from the bulge configuration of a rough interface. The $(321)_{\mathrm{B2}}||(112)_{\mathrm{FCC}}$ shows a fully-coherent characteristic with atomic sites well-matched without bulges, while the interface, q, $(23\bar{1})_{\mathrm{B2}}||(552)_{\mathrm{FCC}}$, exhibits a bulged feature with atomic vacancies. These bulges with atomic vacancies at the interface will lead to stress concentration, when two relaxed surfaces are coupled with each other to form the hetero-phase interface. Thus, it can be inferred that the $(23\bar{1})_{\mathrm{B2}}||(552)_{\mathrm{FCC}}$ interface, q, which is present only along with the growth twin in the EHEA, is not as stable as $(321)_{\mathrm{B2}}||(112)_{\mathrm{FCC}}$. Similarly, the atomistic structure of the $(01\bar{1})_{\mathrm{B2}}||(33\bar{2})_{\mathrm{FCC}}$ interface, presented in Fig. 9(n), also possesses bulges and should have a relatively-high interface energy. However, as commented by Fecht and Gleiter [29], the parallelism between the close-packed directions will lead to a low energy interface. To make a quantitative analysis, we define the sum of the misfit angles between two pairs of contacting close-packed facets as the "facet deviation angle, φ". As shown in Fig. 9(b), the $(321)_{\mathrm{B2}}||(112)_{\mathrm{FCC}}$ interface has a lower facet-deviation angle with the value of $\varphi_{\mathrm{f}} = 5.26^\circ$ than that of the $(23\bar{1})_{\mathrm{B2}}||(552)_{\mathrm{FCC}}$ ($\varphi_{\mathrm{q}} = 11.26^\circ$) and $(01\bar{1})_{\mathrm{B2}}||(33\bar{2})_{\mathrm{FCC}}$ ($\varphi_{\mathrm{n}} = 11.54^\circ$), in agreement with our experimental observation of the dominant role of the $(321)_{\mathrm{B2}}||(112)_{\mathrm{FCC}}$ interface.

In general, in the growth process of the EHEA, the interface, $(321)_{\mathrm{B2}}||(112)_{\mathrm{FCC}}$, with the lowest energy will form with priority. However, considering the complicated circumstance during the fabrication process of the eutectic alloy, the solidification and growth of the alloy deviate from the equilibrium state with a large supercooling degree. The formation of higher energy interfaces, $(23\bar{1})_{\mathrm{B2}}||(552)_{\mathrm{FCC}}$ and $(01\bar{1})_{\mathrm{B2}}||(33\bar{2})_{\mathrm{FCC}}$, may be attributed to the growth perturbation, such as temperature gradients and constituent fluctuations, of the low-energy interface.

4.2. Good ductility owing to the slip continuity across the KS interface

As reported in our previous study, the EHEA presented good ductility [18]. The ductility should result from the co-deformation between B2 and FCC lamellae. Fig. 10(a and b) shows SEM images of the EHEA before (Fig. 10(a)) and after (Fig. 10(b)) a tensile test, as reported in our previous study [18]. No macroscopic strain localization, such as the shear band or layer kinking, can be observed in the deformed EHEA. Further EBSD analysis in Fig. 10(c and d) reveals that the OR remains KS, $<111>_{B2}||<110>_{FCC}$ and $\{110\}_{B2}||\{111\}_{FCC}$, marked with white and red circles, after the tensile test. All these phenomena demonstrate that the B2 and FCC lamellae can deform compatibly on the macroscopic scale. Moreover, the co-deformation behavior in the EHEA relies on the slip transmission between the two phases.

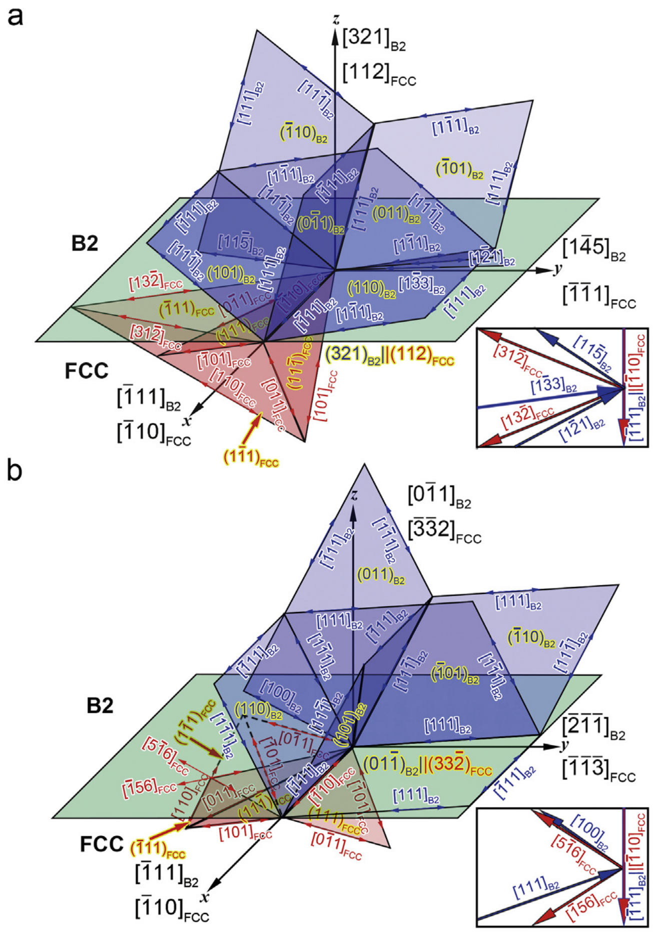

Fig. 11. The geometrical relationships among slip systems of the B2 and FCC phases with respect to two typical interfaces: (a) interface $(321)_{B2}||(112)_{FCC}$; (b) interface $(01\bar1)_{B2}||(33\bar2)_{FCC}$. The sketch maps showing that the intersection lines between the interfaces and the slip planes of the B2 and FCC phases are at the bottom right corner in (a and b).

We consider the geometrical compatibility among the operative slip systems of the B2 and FCC phases under the KS OR with respect to the two primary interfaces, $(321)_{B2}||(112)_{FCC}$ and$(01\bar1)_{B2}||(33\bar2)_{FCC}$, as described below, to reveal the co-deformation mechanism. The geometric relationships are schematically presented in Fig. 11, considering the $\{111\}<110>$ slip systems of the FCC phase and the $\{110\}<111>$ slip systems of the B2 phase. The feasibility of the slip transmission can be quantified by the slip-transfer geometric factor, χ, expressed as,

$$\chi = \left\langle \cos\left(\frac{\pi}{2}\frac{\theta}{\theta_c}\right)\right\rangle \cdot \left\langle \cos\left(\frac{\pi}{2}\frac{\kappa}{\kappa_c}\right)\right\rangle \tag{3}$$

where θ is the angle between the intersection lines that each slip plane makes with the interface, κ is the angle between the Burgers vectors of the incoming and outgoing dislocations, $\theta_c = 15°$ and $\kappa_c = 45°$ are the limiting angles for θ and κ, respectively, and the brackets $\langle\rangle$ mean that when either θ or κ exceeds their limit, θ_c or κ_c, the quantity equals zero [27]. A greater value of χ corresponds to a lower interface obstacle strength and energetically an easier slip transfer across the interface [27]. For each slip system in the FCC phase, most of the piled-up dislocations can transmit across the interface and continue to slip on the paired slip systems in the B2 phase. According to the KS OR between the two phases, Table 3 shows the calculated θ, κ, and χ of the 12 $\{111\}<110>$ slip systems in the FCC phase paired with the corresponding $\{110\}<111>$ slip systems with the maximization χ in the B2 phase. When the maximal χ equals zero, the dislocations in such slip systems in the softer FCC phase are considered to be unable to transmit to the harder B2 phase. From Table 3, no matter the interface presents

Table 3
The θ (the angle between the intersection lines that each slip plane makes with the interface), κ (the angle between the Burgers vectors), and χ (the slip-transfer geometric factor) of the slip system pairs between the B2 and FCC phases.

Slip systems in the FCC phase	Interface: $(321)_{B2}||(112)_{FCC}$				Interface:$(01\bar1)_{B2}||(33\bar2)_{FCC}$			
	Paired slip systems in B2	θ (º)	κ (º)	χ	Paired slip systems in B2	θ (º)	κ (º)	χ
$(111)[\bar101]_{FCC}$	$(110)[1\bar11]_{B2}$	0	49.5	0	$(110)[1\bar11]_{B2}$	0	49.5	0
$(111)[0\bar11]_{FCC}$	$(110)[1\bar11]_{B2}$	0	10.5	0.93	$(110)[1\bar11]_{B2}$	0	10.5	0.93
$(111)[\bar110]_{FCC}$	$(101)[\bar111]_{B2}$	0	0	1	$(101)[\bar111]_{B2}$	0	0	1
	$(0\bar11)[\bar111]_{B2}$	0	0	1	$(0\bar11)[\bar111]_{B2}$	0	0	1
	$(110)[\bar111]_{B2}$	0	0	1	$(110)[\bar111]_{B2}$	0	0	1
$(11\bar1)[011]_{FCC}$	$(0\bar11)[111]_{B2}$	0	14.2	0.88	$(0\bar11)[111]_{B2}$	0	14.2	0.88
$(11\bar1)[101]_{FCC}$	$(101)[11\bar1]_{B2}$	0	45.8	0	$(101)[11\bar1]_{B2}$	0	45.8	0
$(11\bar1)[\bar110]_{FCC}$	$(101)[\bar111]_{B2}$	0	0	1	$(101)[\bar111]_{B2}$	0	0	1
	$(0\bar11)[\bar111]_{B2}$	0	0	1	$(0\bar11)[\bar111]_{B2}$	0	0	1
	$(110)[\bar111]_{B2}$	0	0	1	$(110)[\bar111]_{B2}$	0	0	1
$(\bar111)[110]_{FCC}$	$(011)[11\bar1]_{B2}$	14.6	20.1	0.03	$(011)[11\bar1]_{B2}$	2.7	20.1	0.73
$(\bar111)[101]_{FCC}$	$(011)[11\bar1]_{B2}$	14.6	45.8	0	$(011)[11\bar1]_{B2}$	2.7	45.8	0
$(\bar111)[0\bar11]_{FCC}$	$(\bar101)[1\bar11]_{B2}$	5.9	10.5	0.76	$(011)[1\bar11]_{B2}$	2.7	10.5	0.90
$(1\bar11)[110]_{FCC}$	$(\bar110)[11\bar1]_{B2}$	11.6	20.1	0.27	$(\bar110)[11\bar1]_{B2}$	13.1	20.1	0.15
$(1\bar11)[011]_{FCC}$	$(\bar110)[111]_{B2}$	11.6	14.2	0.31	$(\bar110)[111]_{B2}$	0	14.2	0.88
$(1\bar11)[\bar101]_{FCC}$	$(\bar110)[111]_{B2}$	11.6	49.5	0	$(\bar101)[1\bar11]_{B2}$	13.1	49.5	0

*For each activated slip systems in the FCC phase, the paired slip systems in the B2 phase is selected in 12 $\{110\}\langle111\rangle_{B2}$ slip systems with the maximal χ.
*When the maximal χ equals 0, the dislocations on such slip systems in the FCC phase are considered unable to transmit into the B2 phase.

$(321)_{B2}||(112)_{FCC}$ or $(01\bar{1})_{B2}||(33\bar{2})_{FCC}$, as we can see that 2/3 dislocations of the 12 {111}<110> systems in the FCC phase can penetrate into the B2 phase.

The plastic co-deformation can be rationalized as follows. When the external stress is applied to the EHEA, abundant dislocations will nucleate at the interfaces due to the high stress concentration there. The dislocations preferentially propagate in the softer FCC phase with a lower lattice-friction stress, leading to the plastic deformation of the soft FCC phase. Due to the higher elastic modulus of the B2 phase, the B2 phase firstly deform elastically, and the dislocations will firstly pile up at the B2-FCC interface and cause the stress concentration on certain planes and directions of the B2 lamellae. As mentioned above, two kinds of slip systems associated with {110}<111> and {110}<001> could be activated in the polycrystalline B2 structure, when it deforms at room temperature, as reported in the preceding papers [35,36]. When the activated vector is <001 >, the plastic strain is only less than 2% [40]. The reason is thought to be associated with an insufficient number of independent deformation modes to satisfy the von Mises plasticity criterion for the homogeneous polycrystalline flow [40,41]. The geometries of both the $(321)_{B2}||(112)_{FCC}$ and $(01\bar{1})_{B2}||(33\bar{2})_{FCC}$ interfaces favor the generation of <111> dislocations other than <001> dislocations with more maximum χ values, considering the 12 {110}<111> slip systems in the FCC phase (see the Supplementary Table 1 for details). When the activated Burgers vector is <111 >, the deformability can be improved by the availability of the 12 slip systems. By initiating the {110}<111> slip systems in the B2 phase, most of the accumulated dislocations at the B2-FCC interfaces on the FCC side can be transmitted to the B2 phase to realize the plastic co-deformation of the EHEA.

Moreover, the atomistic-scale interface structure plays an important role on the dislocation-interface interaction, such as the dislocation nucleation and dislocation transmission [42,43]. Usually, the interfaces can be either flat or faceted, according to their atomistic-scale interface characteristics [43–45]. Firstly, compared with the flat interface, the faceted interfaces are more effective sources of dislocations due to a lower activation barrier for dislocation nucleation according to experimental and atomistic simulation studies of the Cu-Nb bimetallic layered composites [43,46]. As a result, the faceted interface can provide abundant dislocations for the subsequent deformation. Meanwhile, previous atomistic simulations show that the FCC-BCC interfaces composed of slip planes with flat atomistic-scale structures, referred to as “weak” interfaces, are ready to shear due to dislocation-core spreads within the interface, leading to interfacial sliding, and are effective barriers for the slip transmission [27,42,47]. Vice versa, the faceted interfaces composed of non-slip planes are reported to be hard to shear and ready to transfer the dislocation slip [27,43]. In the present EHEA, the typical interfaces, $(321)_{B2}||(112)_{FCC}$ and $(01\bar{1})_{B2}||(33\bar{2})_{FCC}$, both are faceted on the atomistic scale, as shown in Fig. 5(a and b), which are beneficial to the dislocation nucleation and slip transmission, resulting in the high ductility.

4.3. *High strength owing to the KS-interface strengthening*

The dual-phase EHEA is supposed to possess the benefits of both the high strength of the B2 phase and the good ductility of the FCC phase. Except for the strengthening effects from the composite reinforcement, it is believed that the prevalent existing hetero-phase interfaces contribute to the strength of the EHEA dramatically. In the following section, the interfacial effects on the strength of the EHEA will be discussed.

According to the aligned slip systems of the B2 and FCC phases and the non-slip plane feature of the interfaces, the dislocations in the FCC phase transmit to the B2 phase in a hard mode with both the slip plane and the Burgers vector forming an angle with the interface. Thus, the interface can act as obstacles of the slip transfer across the interface, as presented in Fig. 8(a). The lamellar thicknesses of the B2 and FCC phases are on the micrometer scale. Thus, similar to multilayer metals, the yield stress is supposed to obey the Hall-Petch relationship according to the continuum dislocation pile-up theory [48]. In dual-phase lamellar systems, the interface-strengthening effects concerning the dislocation-interface interaction, mainly stem from the shear-modulus- and lattice-parameter-mismatch strengthening [49–53]. The different elastic moduli between adjacent phases will exert an extra force to a dislocation in the softer phase to transmit to the harder phase [54,55]. The dislocation near the interface in the FCC phase generates a strain field extending into both the B2 and FCC phases. The strain energy in the B2 phase is larger per unit length because its elastic modulus is greater. Therefore, in order to reduce the energy of the system, an extra force generates to repel the piled-up dislocation in the FCC phase from the interface. In the present case, the elastic moduli of the B2 and FCC phases measured by nanoindentation are 216.42 ± 11.03 GPa and 182.44 ± 13.37 GPa, respectively. The shear modulus, G, can be calculated using the equation [56],

$$G = \frac{E}{2(1+\upsilon)} \tag{4}$$

where E is the elastic modulus, and υ is the Poisson’s ratio. The shear moduli of the B2 and FCC phases are calculated to be 86.57 ± 4.41 GPa and 72.98 ± 5.35 GPa, respectively, with a Poisson’s ratio of 0.25. The shear modulus of the B2 phase is much larger than that of the FCC phase. The greater the difference in the shear moduli between the alternate layers, the greater resistance to the piled-up dislocations will generate [54].

At the same time, interfacial strengthening at the B2-FCC interface also derives from the lattice-parameter mismatch [55]. In general, the difference of the lattice parameters of the adjacent phases at the interface can be accommodated partly by uniformly-distributed misfit dislocations and partly by coherency strains [57]. From Fig. 5(a and b), we can see that there are no misfit dislocations at the $(321)_{B2}||(112)_{FCC}$ interface while one set of regularly-distributed misfit dislocations are found at the $(01\bar{1})_{B2}||(33\bar{2})_{FCC}$ interface. Both the coherency strain and the misfit dislocations interact with the piled-up dislocations by exerting the direct force as well as altering the core structure of the dislocation, which help strengthen the materials.

5. Conclusions

The present work characterized the OR and interface structures and revealed the interface-dominated deformation mechanisms in the $AlCoCrFeNi_{2.1}$ EHEA by combining SEM, EBSD, and TEM techniques. Based on our investigation, the following conclusions can be drawn.

(1) The OR between B2 and FCC phases in the EHEA has been determined to be KS OR with $<111>_{B2}||<110>_{FCC}$ and $\{110\}_{B2}||\{111\}_{FCC}$. This OR has two variants due to the growth twin in the FCC phase.
(2) The EHEA displays three kinds of interfaces, namely $(321)_{B2}||(112)_{FCC}$, $(01\bar{1})_{B2}||(33\bar{2})_{FCC}$, and $(23\bar{1})_{B2}||(552)_{FCC}$. The dominant $(321)_{B2}||(112)_{FCC}$ and secondary $(01\bar{1})_{B2}||(33\bar{2})_{FCC}$ both exhibit atomistic-scale faceted and non-slip plane characteristics. Also, the formation of the dominating $(321)_{B2}||(112)_{FCC}$ interface has been explained by the atomistic geometrical analysis according to the criteria of the low interfacial energy based on the CSL theory.
(3) Based on the atomistic features of the interfaces and the geometrical analysis of the slip systems across the B2-FCC inter-

faces, the faceted KS interfaces facilitate the slip transfer from the FCC phase to the B2 phase and help realize the plastic co-deformation of the two constituent phases in the EHEA. Moreover, the interface strengthening is attributed to the modulus and lattice-parameter mismatches.

Acknowledgments

The present work was supported financially by the National Natural Science Foundation of China (No. 51771201 and No. 51822402), the Key Project of Natural Science Foundation of Liaoning Province, China (No. 20180510059), the Shenyang National Laboratory for Materials Science (No. 2017RP17), and the State Key Laboratory of Solidification Processing in Northwestern Polytechnical University (No. SKLSP201902). The authors also thank Prof. Jian Wang at Department of Mechanical and Materials Science Engineering, University of Nebraska, Lincoln for helpful discussions. PKL very much appreciates the support of the U.S. Army Research Office Project (W911NF-13-1-0438 and W911NF-19-2-0049) with the program managers, Drs. M. P. Bakas, S. N. Mathaudhu, and D. M. Stepp. PKL thanks the support from the National Science Foundation (DMR-1611180 and DMR-1809640) with the program directors, Drs. J. Yang, G. Shiflet, and D. Farkas.

Appendix A. Supplementary data

Supplementary material related to this article can be found, in the online version, at doi:https://doi.org/10.1016/j.jmst.2020.04.073.

References

[1] J.W. Yeh, S.K. Chen, S.J. Lin, J.Y. Gan, T.S. Chin, T.T. Shun, C.H. Tsau, S.Y. Chang, Adv. Eng. Mater. 6 (2004) 299–303.
[2] Y. Zhang, T.T. Zuo, Z. Tang, M.C. Gao, K.A. Dahmen, P.K. Liaw, Z.P. Lu, Prog. Mater. Sci. 61 (2014) 1–93.
[3] F. Otto, Y. Yang, H. Bei, E.P. George, Acta Mater. 61 (2013) 2628–2638.
[4] M.J. Yao, K.G. Pradeep, C.C. Tasan, D. Raabe, Scr. Mater. 72-73 (2014) 5–8.
[5] H. Shen, J. Hu, P. Li, G. Huang, J. Zhang, J. Zhang, Y. Mao, H. Xiao, X. Zhou, X. Zu, X. Long, S. Peng, J. Mater. Sci. Technol. (2020), http://dx.doi.org/10.1016/j.jmst.2019.08.060, In Press.
[6] M. Sahlberg, D. Karlsson, C. Zlotea, U. Jansson, Sci. Rep. 6 (2016) 36770.
[7] M.A. Hemphill, T. Yuan, G.Y. Wang, J.W. Yeh, C.W. Tsai, A. Chuang, P.K. Liaw, Acta Mater. 60 (2012) 5723–5734.
[8] Z. Tang, T. Yuan, C.W. Tsai, J.W. Yeh, C.D. Lundin, P.K. Liaw, Acta Mater. 99 (2015) 247–258.
[9] Y.P. Lu, H.F. Huang, X.Z. Gao, C.L. Ren, J. Gaob, H.Z. Zhang, S.J. Zheng, Q.Q. Jin, Y.H. Zhao, C.Y. Lu, T.M. Wang, T.J. Li, J. Mater. Sci. Technol. 35 (2019) 369–373.
[10] L.X. Yang, H.L. Ge, J. Zhang, T. Xiong, Q.Q. Jin, Y.T. Zhou, X.H. Shao, B. Zhang, Z.W. Zhu, S.J. Zheng, X.L. Ma, J. Mater. Sci. Technol. 35 (2019) 300–305.
[11] Y.W. Zhang, G.M. Stocks, K. Jin, C.Y. Lu, H.B. Bei, B.C. Sales, L.M. Wang, L.K. Beland, R.E. Stoller, G.D. Samolyuk, M. Caro, A. Caro, W.J. Weber, Nat. Commun. 6 (2015) 8736.
[12] W. Chen, X. Ding, Y. Feng, X. Liu, K. Liu, Z.P. Lu, D. Li, Y. Li, C.T. Liu, X.Q. Chen, J. Mater. Sci. Technol. 34 (2018) 355–364.
[13] Y.F. Ye, Q. Wang, J. Lu, C.T. Liu, Y. Yang, Mater. Today 19 (2016) 349–362.
[14] O.N. Senkov, G.B. Wilks, J.M. Scott, D.B. Miracle, Intermetallics 19 (2011) 698–706.
[15] B. Gludovatz, A. Hohenwarter, D. Catoor, E.H. Chang, E.P. George, R.O. Ritchie, Science 345 (2014) 1153–1158.
[16] T.T. Shun, Y.C. Du, J. Alloys Compd. 479 (2009) 157–160.
[17] L. Wang, C. Yao, J. Shen, Y. Zhang, T. Wang, Y. Ge, L. Gao, G. Zhang,Intermetallics 118 (2020), 106681.
[18] Y.P. Lu, X.Z. Gao, L. Jiang, Z.N. Chen, T.M. Wang, J.C. Jie, H.J. Kang, Y.B. Zhang, S. Guo, H.H. Ruan, Y.H. Zhao, Z.Q. Cao, T.J. Li, Acta Mater. 124 (2017) 143–150.
[19] I.S. Wani, T. Bhattacharjee, S. Sheikh, Y.P. Lu, S. Chatterjee, P.P. Bhattacharjee, S. Guo, N. Tsuji, Mater. Res. Lett. 4 (2016) 174–179.
[20] I.S. Wani, T. Bhattacharjee, S. Sheikh, P.P. Bhattacharjee, S. Guo, N. Tsuji, Mater. Sci. Eng. A. 675 (2016) 99–109.
[21] P. Shi, W. Ren, T. Zheng, Z. Ren, X. Hou, J. Peng, P. Hu, Y. Gao, Y. Zhong, P.K. Liaw, Nat. Commun. 10 (2019) 489.
[22] H. Zheng, R. Chen, G. Qin, X. Li, Y. Su, H. Ding, J. Guo, H. Fu,Intermetallics 113 (2019), 106569.
[23] X. Gao, Y. Lu, B. Zhang, N. Liang, G. Wu, G. Sha, J. Liu, Y. Zhao, Acta Mater. 141 (2017) 59–66.
[24] B.P. Eftink, A. Li, I. Szlufarska, N.A. Mara, I.M. Robertson, Acta Mater. 138 (2017) 212–223.
[25] J. Wang, I.J. Beyerlein, N.A. Mara, D. Bhattacharyya, Scr. Mater. 64 (2011) 1083–1086.
[26] B.P. Eftink, A. Li, I. Szlufarska, I.M. Robertson, Acta Mater. 117 (2016) 111–121.
[27] S.J. Zheng, J. Wang, J.S. Carpenter, W.M. Mook, P.O. Dickerson, N.A. Mara, I.J. Beyerlein, Acta Mater. 79 (2014) 282–291.
[28] A. Day, P. Trimby, Channel 5 Manual, HKL Technology Inc., Denmark, 2004.
[29] H.J. Fecht, H. Gleiter, Acta Metall. 33 (1985) 557–562.
[30] S. Ranganathan, Acta Crystallogr. 21 (1966) 197–199.
[31] A.P. Sutton, R.W. Balluffi, Acta Metall. 35 (1987) 2177–2201.
[32] A. Stukowski,Modelling Simul. Mater. Sci. Eng. 18 (2010), 015012.
[33] G. Kurdjumow, G. Sachs, Z. Phys. 64 (1930) 325–343.
[34] S. Morito, H. Tanaka, R. Konishi, T. Furuhara, T. Maki, Acta Mater. 51 (2003) 1789–1799.
[35] A. Ball, R.E. Smallman, Acta Metall. 14 (1966) 1517–1526.
[36] C.L. Fu, M.H. Yoo, Acta Metall. Mater. 40 (1992) 703–711.
[37] H. Saka, M. Kawase, Philos. Mag. A 49 (1984) 525–533.
[38] A.T. Jennings, J.R. Greer, J. Mater. Res. 26 (2011) 2803–2814.
[39] R.F. Zhang, J. Wang, I.J. Beyerlein, T.C. Germann, Scr. Mater. 65 (2011) 1022–1025.
[40] K.H. Hahn, K. Vedula, Scr. Metall. 23 (1989) 7–12.
[41] R.V. Mises, Z. Angew. Math. Mech. 8 (1928) 161–185.
[42] R.F. Zhang, I.J. Beyerlein, S.J. Zheng, S.H. Zhang, A. Stukowski, T.C. Germann, Acta Mater. 113 (2016) 194–205.
[43] R.F. Zhang, T.C. Germann, J. Wang, X.Y. Liu, I.J. Beyerlein, Scr. Mater. 68 (2013) 114–117.
[44] S.J. Zheng, J.S. Carpenter, R.J. McCabe, I.J. Beyerlein, N.A. Mara, Sci. Rep. 4 (2014).
[45] S.J. Zheng, I.J. Beyerlein, J.S. Carpenter, K.W. Kang, J. Wang, W.Z. Han, N.A. Mara, Nat. Commun. 4 (2013) 1696.
[46] S.J. Zheng, I.J. Beyerlein, J. Wang, J.S. Carpenter, W.Z. Han, N.A. Mara, Acta Mater. 60 (2012) 5858–5866.
[47] J. Wang, R.G. Hoagland, J.P. Hirth, A. Misra, Acta Mater. 56 (2008) 5685–5693.
[48] A. Misra, J.P. Hirth, R.G. Hoagland, Acta Mater. 53 (2005) 4817–4824.
[49] J.D. Eshelby, F.C. Frank, F.R.N. Nabarro, Philos. Mag. 42 (1951) 351–364.
[50] J.S. Koehler, Phys. Rev. B 2 (1970) 547–551.
[51] D.M. Martin, T.D. McGee, Acta Metall. 17 (1969) 929–932.
[52] R.G. Hoagland, R.J. Kurtz, C.H. Henager, Scr. Mater. 50 (2004) 775–779.
[53] G. Qin, R. Chen, P.K. Liaw, Y. Gao, X. Li, H. Zheng, L. Wang, Y. Su, J. Guo, H. Fu, Scr. Mater. 172 (2019) 51–55.
[54] S.I. Rao, P.M. Hazzledine, D.M. Dimiduk, Mater. Res. Soc. Symp. Proc. 362 (1995) 67–77.
[55] S.I. Rao, P.M. Hazzledine, Philos. Mag. A 80 (2000) 2011–2040.
[56] S.M. Chung, A.U.J. Yap, W.K. Koh, K.T. Tsai, C.T. Lim, Biomaterials 25 (2004) 2455–2460.
[57] G.B. Olson, M. Cohen, Acta Metall. 27 (1979) 1907–1918.